ACS Catalysis

Research Article

pubs.acs.org/acscatalysis

Imaging the Site-Specific Activity and Kinetics on a Single Nanomaterial by Microchamber Array

Ying Du,[†,‡] Xudong He,[‡,§] Yulu Zhan,[†,‡] Shuping Li,[‡,∥] Yangbin Shen,[‡,∥] Fandi Ning,[‡,⊥] Liuming Yan,[†] and Xiaochun Zhou*[,‡,#]

[†]Department of Chemistry, College of Sciences, Shanghai University, 99 Shangda Road, Shanghai 200444, People's Republic of China

[‡]Division of Advanced Nanomaterials, Suzhou Institute of Nano-tech and Nano-bionics, Chinese Academy of Sciences, Suzhou 215125, People's Republic of China

[§]Wuhan University, Wuhan 430071, People's Republic of China

[∥]University of Chinese Academy of Sciences, Beijing 100049, People's Republic of China

[⊥]University of Science and Technology of China, Hefei 230026, People's Republic of China

[#]Key Laboratory of Nanodevices and Applications, Suzhou Institute of Nano-tech and Nano-bionics, Chinese Academy of Sciences, Suzhou 215125, People's Republic of China

Supporting Information

ABSTRACT: One-dimensional (1D) and two-dimensional (2D) nanomaterials usually show diverse catalytic activities at different locations. For a particular location, the local reaction activity could be too fast to be measured by super-resolution microscopy (SRM). To solve this problem, this research uses a large array of polydimethylsiloxane (PDMS) microchambers to resolve the site-specific activity on a single gold nanoplate with micrometer resolution, in situ and in real time. This research presents a general method to screen the catalytic activity distribution on single nanomaterials, even if the local activity is up to TOF = 5.9 × 10^5 s^{-1}, the adsorption time of the fluorescent molecule is short, and fluorescence quenching occurs on the nanomaterials. This research reveals that the site-specific activities of different regions on a single gold nanoplate follows the trend corner > edge > flat facet. This research also reveals that the site-specific activities of the flat facet and corner regions are not dependent on the size of the gold nanoplate, while the site-specific activity of the edge region is positively dependent on the size. The positive correlation is due to the increasing roughness of the edges with the size of the gold nanoplates. Larger roughness indicates more defects with higher reactivity. In addition, we found two kinds of catalytic kinetic pathways: i.e., the direct pathway and the indirect pathway. We further studied the effect of the size, region, and shape of the gold nanoplate on the direct pathway. Finally, the approach developed in this research exhibits many advantages, including high sensitivity, low reagent consumption, reusability, and recyclability, which make it generally applicable in many other types of reactions, including electrochemical and photochemical reactions.

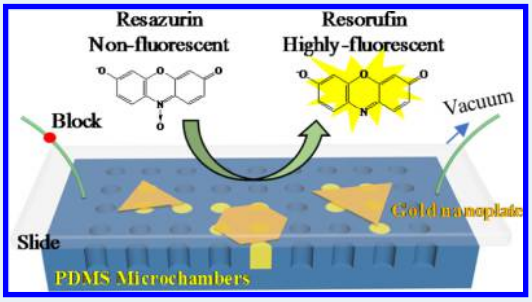

KEYWORDS: *single nanoparticle, PDMS microchamber, gold nanoplate, site-specific activity, catalytic kinetics*

1. INTRODUCTION

One-dimensional (1D) and two-dimensional (2D) nanomaterials have attracted considerable interest due to their outstanding physical and chemical properties.[1−4] So far, various 1D and 2D nanomaterials, such as carbon nanotubes,[5−7] graphene,[8,9] transition-metal dichalcogenides (TMDs),[10−12] Au nanosheets,[13−15] and TiO_2 nanoplates,[16,17] have been successfully synthesized. These 1D and 2D nanomaterials are usually smaller than 100 nm in at least one dimension but could be larger in size in other dimensions. For example, the length of Ag nanowires and carbon nanotubes can reach 2 mm[18] and 0.5 m,[19] respectively, and the size of gold nanoplates can be over 50 μm in edge length.[20,21] These large sizes in a particular dimension facilitate electron transfer with high efficiency over a long distance. This property makes these 1D or 2D nanomaterials perfect catalysts or supports for charge transfer reactions, such as electrochemical,[22−25] photochemical,[26−28] and galvanic replacement reactions.[29,30]

These 1D and 2D nanomaterials usually show highly nonuniform catalytic activity because the facets, structures, defects, and composition are not uniformly distributed throughout the materials.[31−38] For example, by using super-resolution microscopy (SRM), Majima's group found that the distribution of catalytic activity is not uniform on individual

Received: December 11, 2016
Revised: February 26, 2017
Published: March 28, 2017

DOI: 10.1021/acscatal.6b03518
ACS Catal. 2017, 7, 3607−3614

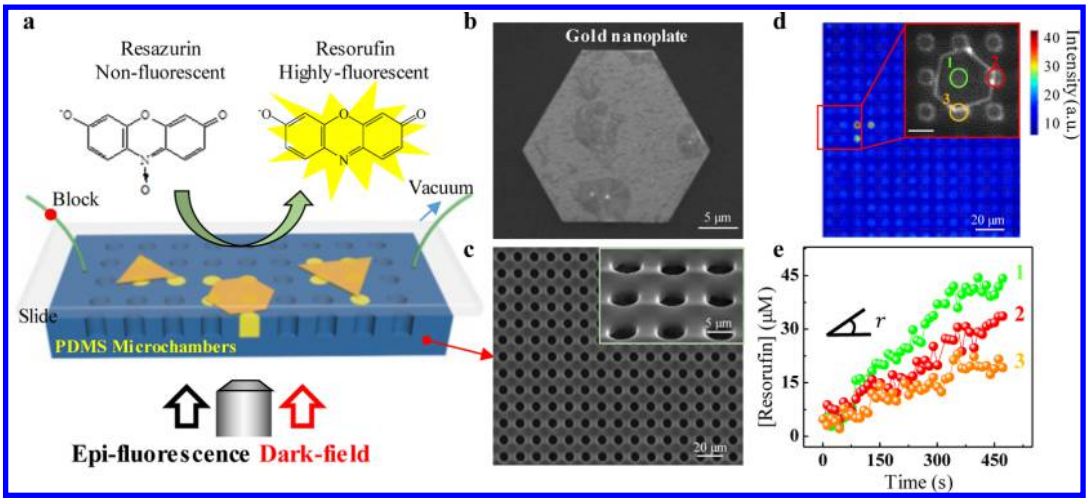

Figure 1. Imaging a fluorogenic reaction on different regions of a single gold nanoplate by using PDMS microchambers. (a) Schematic of the fluorogenic reaction on different regions of a single gold nanoplate occurring in the PDMS microchambers under an integration of dark-field and epifluorescence microscopes. The epifluorescence microscope is mainly used for the detection of fluorescence signals, and the dark-field microscope is mainly for the measurement of the dimensions of the gold nanoplates and microchambers. The yellow microchambers covering certain regions of the gold nanoplates are where the fluorogenic reaction has occurred. (b) SEM image of a typical gold nanoplate. (c) SEM image of an array of micrometer-sized PDMS chambers (5 μm in both diameter and depth). The insert is an enlarged SEM image. (d) Fluorescence intensity of the microchamber array after reaction for about 1554 s. The microchambers with higher fluorescence intensity in the red square cover different regions of an individual hexagonal gold nanoplate, which is shown in the dark-field image in the inset. (e) Fluorescence intensity versus time trajectories of the PDMS microchambers circled with different colors and marked with different numbers, as shown in (d). To clearly illustrate the linear increase of fluorescence intensity with time at the beginning of the reaction, we only show the initial 450 s. In this figure, r represents the initial reaction rate.

micrometer-level TiO_2 nanosheets. They found that there were some hot spots of the photocatalytic reaction. When the hot spots were compared to the SEM images of the crystals, they were observed to be strongly associated with surface damage.[37] In addition to the intrinsic nonuniform catalytic activity, researchers can selectively functionalize different locations on the 1D and 2D nanomaterials by controlling the deposition of different types of catalysts on them. These kinds of catalysts could possess much higher activity in both photocatalytic and photoelectrocatalytic water oxidation reactions in comparison to that of a photocatalyst with randomly distributed catalysts.[39]

To understand the reaction mechanism and optimize the performance of catalysts, it is necessary to map the activity distribution on single nanomaterials and determine the corresponding structure, facets, and composition locally. At present, SRM is one of the most effective ways to map the site-specific activity of a single nanoparticle with several tens of nanometers resolution in situ and in real time.[32,35−37,40−43] Roeffaers' group used SRM to map the epoxidation activity of Ti-MCM-41 for large substrates.[41] The results confirmed that only a restricted portion of Ti on the common micrometer-sized Ti-MCM-41 particles contributes to the observed activity. Using SRM, Chen's group found that the catalytic activity within the flat surface facet of a gold nanoplate exhibits a 2D radial gradient from the center toward the periphery.[40] They proposed that this activity gradient results from a growth-dependent surface defect distribution.

However, it is difficult to use the SRM method to study high-activity reactions involving a single molecule (TOF > 1000 s^{-1}) because the time resolution limit of highly sensitive cameras (e.g., the EMCCD camera) is several milliseconds. In addition, SRM is also hard to use if the adsorption time of the fluorescent molecule is too short or if fluorescence quenching occurs on the nanomaterials. Therefore, developing new methods is still needed to map the activity distribution on single nanomaterials.

Here, we use a large array of polydimethylsiloxane (PDMS) microchambers to image the site-specific activity and kinetics on a single 2D gold nanoplate by using an integration of dark-field and epifluorescence microscopy. The PDMS microchamber array can trap the reactants and the products for the detection of fluorescence signals and can also divide an individual gold nanoplate into different regions, including flat facet, edge, and corner. This research presents a general method to study the catalytic activity distribution on single nanomaterials, even if the measurement is difficult for SRM. Moreover, the approach invented in this research has many other advantages, including high sensitivity, low reagent consumption, reusability, and recyclability. It also provides an attractive platform to image site-specific activity and kinetics on many other single 1D or 2D nanomaterials and for many other types of reactions, including electrochemical and photochemical reactions.

2. RESULTS AND DISCUSSION

2.1. Imaging Fluorogenic Reactions with PDMS Microchambers. PDMS microreactor arrays were originally applied in the biology field to study single enzymes,[44] single rotary molecular motor proteins,[45] DNA sequencing,[46] and single-cell drug efflux activity.[47] In this research, a large array of micrometer-sized PDMS chambers (98 fL in volume for each microchamber) was used to image the activities at different regions of individual gold nanoplates (Figure 1a and Figures S1−S3 in the Supporting Information). Some micrometer-scale gold nanoplates with 5−30 μm edge length and ∼30 nm thickness[48] (Figure 1b, bright-field image in Figure S5 in the Supporting Information, UV−vis−NIR absorption spectrum in Figure S6 in the Supporting Information, TEM images in Figure S7 in the Supporting Information, and AFM images in Figure S8 in the Supporting Information) were used as catalysts for the catalytic reaction. The shapes of the nanoplates included

DOI: 10.1021/acscatal.6b03518
ACS Catal. 2017, 7, 3607−3614

hexagons, triangles, ladder, and other shapes (Figures S5−S10 in the Supporting Information). The PDMS microchambers, which contained the reactants of 100 μM resazurin and 0.1 M NH_2OH, were used as microreactors (Figure 1c). The microchambers covering certain regions of gold nanoplates carried out a fluorogenic reaction converting nonfluorescent resazurin (R) to the highly fluorescent product resorufin (P) (yellow chambers in Figure 1a and high-intensity chambers in Figure 1d). A circularly polarized 532 nm laser (~5−10 μW) was focused onto the array of microchambers every 1 s for 10 s to directly excite the fluorescence of the product resorufin molecules. The fluorescence signal was recorded by an EMCCD camera in an epifluorescence microscope (Figure 1a,d; the equipment is shown in Figure S4 in the Supporting Information).

Figure 1d shows that the fluorescence intensity in three of the PDMS microchambers sharply increases after a reaction of about 1554 s. When we checked the corresponding dark-field image (insert in Figure 1d), we found that these microchambers always covered certain regions of the single gold nanoplates. Figure 1d clearly shows that these three microchambers with high fluorescence intensity match three different regions of an individual hexagonal gold nanoplate. Therefore, the PDMS microchambers can be successfully used as microreactors to trap the reactant and fluorescent product molecules for the detection of fluorescence signals.

Figure 1e exhibits the fluorescence intensity versus time trajectories of these three microchambers. All the fluorescence intensities of these three chambers linearly increase with time at the beginning of the reaction. The fluorescence intensity is proportional to the concentration of the product resorufin

$$C_{\text{resorufin}} = p_1 I_f \tag{1}$$

where p_1 is a constant, $C_{\text{resorufin}}$ is the concentration of resorufin, and I_f is the fluorescence intensity. In this research, p_1 is 293 nM due to the fluorescence intensity of 100 μM resorufin being ~341. Thus, the slope of the variation of fluorescence intensity is proportional to the fluorogenic reaction rate r in the microchamber:

$$r = p_1 \frac{dI_f}{dt} \tag{2}$$

Because the concentrations of reactants are as high as 100 μM for resazurin and 0.1 M for NH_2OH, both reactants are in large excess at the beginning of the reaction.[32] According to the Langmuir−Hinshelwood kinetics, the reaction rate equals the catalytic rate constant when the two reactants are all at the saturation state (section SI-12 in the Supporting Information). Considering that the regions covered by microchambers have different surface areas (insert in Figure 1d), the site-specific catalytic rate constant k_r at different regions will be

$$k_r = \left.\frac{r}{A_t}\right|_{t=0} = \left.\frac{p_1}{A_t}\frac{dI_f}{dt}\right|_{t=0} \tag{3}$$

where A_t is the total surface area of the region covered by a microchamber and t is reaction time. Because the time resolution in this paper can reach several tens of microseconds, the microchamber method could study the catalytic activity up to 5.9×10^5 s^{-1}, assuming the reaction is complete in 10 s.

2.2. Site-Dependent Activity on Single Gold Nanoplates. The insert in Figure 2a shows that PDMS microchambers can dissect the single gold nanoplate into different types of regions: flat facet (yellow circle), edge (red circle), and corner (green circle). These regions actually contain different parts of the individual gold nanoplates. The flat facet region (yellow circle) only contains a flat facet of the individual gold nanoplate, the edge region (red circle) contains both a flat facet and edge, and the corner region (green circle) usually contains a flat facet, edge, and corner. Because the average thickness of gold nanoplates is only approximately 30 nm, the surface area of each type of catalytic region is mainly dominated by the flat facets. We determined the specific activity in each type of region using eq 3.

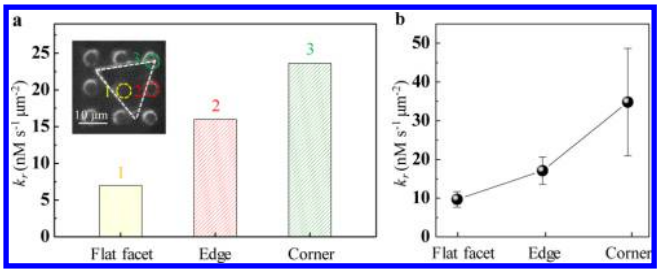

Figure 2. Comparison of the site-specific activities of different types of regions on single gold nanoplates. (a) Site-specific activities of the different types of regions on one example of the individual gold nanoplate. Regions 1−3 are from the individual triangular gold nanoplate in the inset. The yellow, red, and green columns correspond to the regions of flat facet, edge, and corner, respectively. (b) Averaged site-specific activities of 132 regions from 72 gold nanoplates. The error bar is the standard error of the mean.

Figure 2a shows that the specific activity of the corner region is higher than that of the edge region and the specific activity of the edge region is higher than that of the flat facet region for the individual triangular gold nanoplate. When we took the average of a number of gold nanoplates (132 regions of 72 nanoplates in total), the specific activities of different regions follow the trend corner > edge > flat facet (Figure 2b). In addition, the trend is consistent with a previous report[40] and verifies the reliability of the microchamber method presented in this research.

Similar to previous reports,[32,37,40] the site-dependent specific activity can also be rationalized by low-coordination metal sites (e.g., corner, edge, and defect sites on the surface of catalysts) at different regions. These low-coordination metal sites are often more reactive due to their coordinative unsaturation.[49] We know that the coordinative unsaturation of different regions follows the trend corner > edge > flat facet[40] and consequently presents the same trend in specific activity. It is necessary to note that the error bar of the corner regions in Figure 2b is large, indicating a large nonuniform distribution of specific activity on the corner regions, which is due to the nonuniform distribution of low-coordination metal sites. However, the trend corner > edge > flat facet existed in single gold nanoplates (Figure 2a) and was retained after averaging many nanoplates. Therefore, Figure 2b shows a clear trend but with a large error bar.

2.3. Size-Dependent Specific Activity. We further studied the size-dependent specific activity for the different types of regions by calculating the correlation between the specific activity of different regions and the size of gold nanoplates (Figure 3a−c). The correlation coefficients ρ for the flat facet and corner regions are only −0.08 and −0.04, respectively, which indicates that the specific activities of the flat facet and corner regions are independent of the whole size of

DOI: 10.1021/acscatal.6b03518
ACS Catal. 2017, 7, 3607−3614

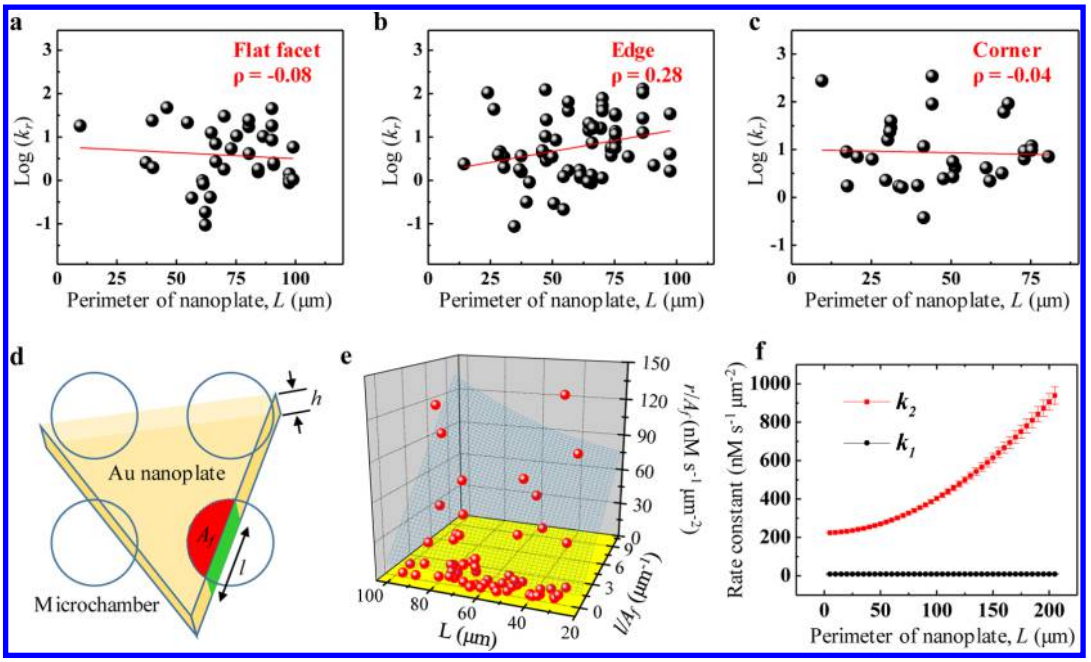

Figure 3. Size-dependent specific activities of different regions. (a) Correlation between the specific activity of the flat facet region and the perimeter of the whole individual gold nanoplate. The correlation coefficient ρ is −0.08. (b) Correlation between the specific activity of the edge region and the perimeter. ρ = 0.28. (c) Correlation between the specific activity of the corner region and the perimeter. ρ = −0.04. (d) Dimension parameters of an individual gold nanoplate. Red and green areas are the flat facet and edge parts, respectively, of a gold nanoplate covered by a microchamber. (e) Fitting of the size-dependent specific activities with eq 7. (f) Plot of k_1 and k_2 versus the perimeter of nanoplates. Because gold nanoplates have diverse shapes, the perimeter was used to represent the size of the gold nanoplates.

the gold nanoplate. The special nanostructures of the flat facet and corner regions may rationalize the independence. Figure S8 in the Supporting Information shows that the surface fluctuation is always within 10 nm over a range of several tens of micrometers. Such a smooth surface has a low possibility of forming low-coordination metal sites with high activities. Moreover, such characteristics of flat facets are not sensitive to the size of the gold nanoplate. The corner region of nanoplates always has abundant low-coordination metal sites, which is active for the reaction. The density of low-coordination metal sites is also not sensitive to the size of the gold nanoplate.

In contrast, there exists a relatively strong positive correlation (ρ = 0.28) between the specific activity of the edge region and the whole size of the gold nanoplate (Figure 3b). In other words, the edge region on larger gold nanoplates exhibits higher reactivity. The edge region includes two parts, which are the flat facet (red area in Figure 3d) and the edge (green area in Figure 3d) of an individual gold nanoplate. Both parts contribute to the activity of the edge region. Because the specific activity of the flat facet is not dependent on the total size of the gold nanoplate, the relatively strong positive correlation of ρ = 0.28 is mainly attributed to the edge of the gold nanoplates.

In the following paragraphs, a semiempirical model is built to interpret the size-dependent specific activity of the edge region. Because the concentrations of reactants are all in the saturation range, the activity of the edge region is linearly proportional to the surface area of the flat facet and the edge of gold nanoplates. Thus, the reaction rate r can be expressed as

$$r = k_1 A_f + k_2 A_e \quad A_e = hl \tag{4}$$

where A_f is the surface area of the flat facet, A_e is the surface area of the edge, k_1 and k_2 are the specific catalytic rate constants at the flat facet and the edge, respectively, h is the thickness of the individual gold nanoplate (Figure 3d), and l is the length of the edge covered by a microchamber (Figure 3d). Because the strong positive correlation ρ = 0.28 mainly contributes to the edge of the gold nanoplate, the specific catalytic rate constant at the edge k_2 is proportional to the total size of the gold nanoplate. It can be expressed as

$$k_2 = \beta L^{\alpha} + k_0 \tag{5}$$

where α and β are constants, L is the perimeter of the individual gold nanoplate (i.e., the size of gold nanoplate), and k_0 is the specific catalytic rate constant at the edge when the size of the gold nanoplates approaches zero (i.e., $L \rightarrow 0$). By combining eqs4 and 5, the reaction rate is

$$r = k_1 A_f + (\beta L^{\alpha} + k_0) hl \tag{6}$$

Then

$$\frac{r}{A_f} = k_1 + (\beta L^{\alpha} + k_0) h \frac{l}{A_f} \tag{7}$$

The dimension parameters, including l, A_f, and h of the individual gold nanoplate, are marked in Figure 3d and can be measured by a dark-field microscope and AFM. In the edge region covered by a microchamber, it is easy to obtain the r/A_f, l/A_f, and h values. Equation 7 was used to fit the size-dependent specific activities in Figure 3e. Through the fitting, we can obtain the following parameter values: α = 1.93 ± 0.13, β = (2.47 ± 0.16) × 10^{-2}, k_0 = 224.0 ± 17.4 nM s^{-1} μm^{-2}, and k_1 = 9.4 ± 4.1 nM s^{-1} μm^{-2}.

The k_1 value (9.4 ± 4.1 nM s^{-1} μm^{-2}) from the fitting agrees well with the value obtained by directly averaging the specific catalytic rate constants (9.7 ± 2.3 nM s^{-1} μm^{-2}) in Figure 2b. Moreover, Figure 3f shows that k_2 (>224.0 ± 17.4 nM s^{-1}

DOI: 10.1021/acscatal.6b03518
ACS Catal. 2017, 7, 3607−3614

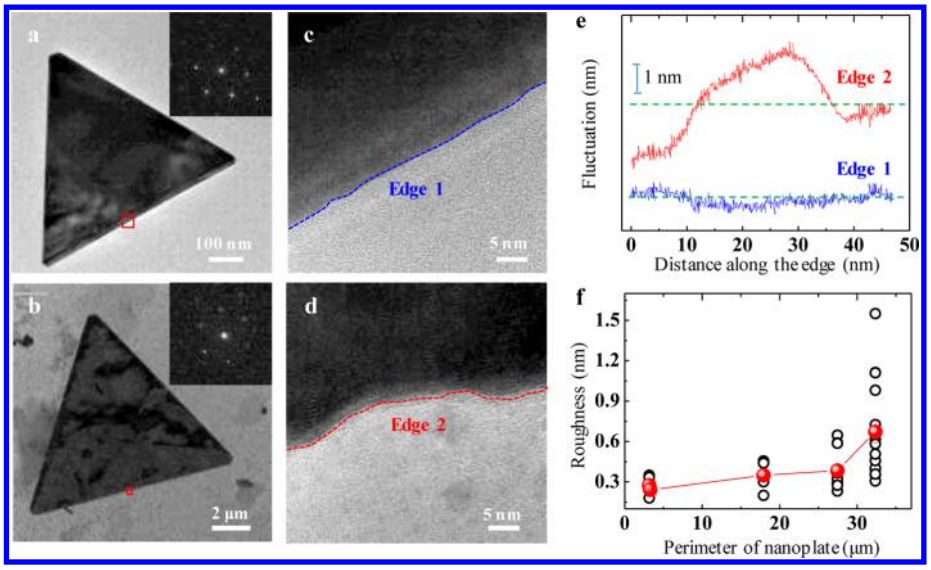

Figure 4. Edge roughness of gold nanoplates with different sizes. (a) TEM image of a typical small gold nanoplate (3.15 μm in perimeter). (b) TEM image of a typical large gold nanoplate (32.3 μm in perimeter). (c) Segment of the edge of the small gold nanoplate in (a). (d) Segment of the edge of the large gold nanoplate in (b). (e) Fluctuation of the edges in (c) and (d). Green lines are the baselines for the two edges. (f) Roughness of edges of the gold nanoplates with different sizes. The black circles are the segments of the gold nanoplates. The red balls are the average values. The inserts in (a) and (b) show the selected area's electron diffraction (SAED) pattern marked by a red square, indicating the same {111} surface facet.

μm^{-2}) keeps increasing with the perimeter of the nanoplate and is always 24−100 times higher than k_1 (9.4 ± 4.1 nM s^{-1} μm^{-2}). Therefore, the reactivity of the edge is much higher than that of the flat facet of gold nanoplates.

To reveal the mechanism for the size-dependent local activity, we took a series of TEM images of gold nanoplates with different sizes, as shown in Figure 4. Figure 4a,b shows the TEM images of typical small and large gold nanoplates, respectively. When we enlarged the area of the edge, we found that the edge of the small gold nanoplate in Figure 4c was rather smooth, while the edge of the large nanoplate in Figure 4d was much rougher. Figure 4e shows the fluctuation of the edges in Figure 4c,d. For the small nanoplate, the fluctuation of the edge is within only 1 nm, while the fluctuation of the edge is up to 4 nm for the large nanoplate. The standard deviation of the fluctuation of the edge was used as the roughness of the edge (Section SI-11 in the Supporting Information).[50] Figure 4f shows that the roughness of edges for different sizes of gold nanoplates increases with the size of the nanoplates. Moreover, the distribution of defect sites was usually not uniform at the edges within one individual gold nanoplate (Figure 4f). Especially for larger gold nanoplates, the difference in the roughness was more obvious (Figure 4f). As a result, catalytic activity at the edge may vary 10 times within one individual plate. The error bar of averaged activity in Figure 2b is consequently large for the edge and corner.

It is well-known that the growth process of gold nanoplates is from the center to the periphery. Larger gold nanoplates usually grow faster than smaller nanoplates during their synthesis process, indicating that they could have more defects from the growth process. These defects are the potential active sites with higher reactivity. Figure 4 clearly shows that the roughness of edges for larger gold nanoplates is much greater than that for smaller gold nanoplates. Therefore, the edges of larger nanoplates have higher reactivity than that of smaller nanoplates.

2.4. Two Types of Catalytic Kinetics. The fluorescence intensity trajectories usually show two types of catalytic kinetics, as shown in Figure 5a,b (more examples are shown in Figures S13 and S14 in the Supporting Information). Figure

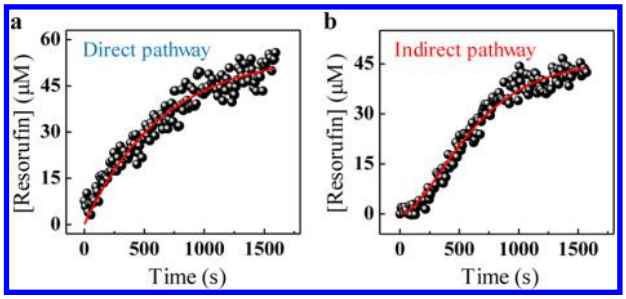

Figure 5. Two types of catalytic kinetics. Fluorescence intensity versus time trajectories following the direct pathway (a) and the indirect pathway (b).

5a shows the first type, where the fluorescence intensity increases sharply at the beginning of the reaction and approaches a limited value afterward. Such behavior indicates that the reaction follows a direct pathway.[51,52] Figure 5b shows the second type, where the fluorescence intensity slowly increases at the beginning of the reaction, then has a sharp increase, and approaches a limited value at the end. Such behavior indicates that this reaction follows an indirect pathway, which may be induced by two possible reasons. One is an intermediate process,[53,54] and the other is an induction process.[52,55,56] For an intermediate process, the reactants need to form intermediates before the formation of product.[53,54] For an induction process, a substrate-induced surface reconstruction is necessary to render the nanoplates as an active catalyst.[52,55,56] Either process will cause a slow reaction rate at the beginning of the reaction. Therefore, the direct pathway usually shows much higher activity than the indirect pathway at the beginning of the reaction.

Most of the regions of gold nanoplates (~89%) follow the direct pathway, and only a small fraction of the regions of gold nanoplates (~11%) follow the indirect pathway. We also find

DOI: 10.1021/acscatal.6b03518
ACS Catal. 2017, 7, 3607−3614

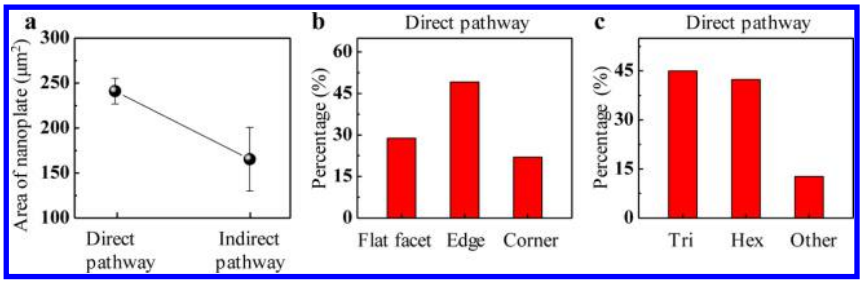

Figure 6. Size, region, and shape distributions for the two types of catalytic kinetics: (a) average total area of individual gold nanoplates for the two types of catalytic kinetics; (b) region distribution of the direct pathway; (c) shape distribution of the direct pathway.

that, for a certain gold nanoplate, only one pathway exists in its different regions. Because the reaction kinetics over time will be affected by many factors, such as competitive binding of the product, byproduct poisoning, and catalyst deactivation, it is very difficult to build a precise kinetic model to fit the kinetic curves in Figure 5a,b.

We further studied the dependence of the two types of catalytic kinetics on the size, region, and shape of gold nanoplates. First, we found that the direct pathway has a higher total surface area for the gold nanoplate than the indirect pathway (Figure 6a). In other words, larger gold nanoplates have a higher possibility to undergo the direct pathway, while more small gold nanoplates have a higher possibility to undergo the indirect pathway. Second, the direct pathway is region dependent, as shown in Figure 6b. The proportion of the edge region for the direct pathway is higher than that of the flat facet and corner regions. Third, the shape dependence of the direct pathway is shown in Figure 6c. The direct pathway's proportions of triangular and hexagonal gold nanoplates are approximately the same and are much higher than that of other shapes. The percentage of distribution of the indirect pathway is not presented here because the sample size for the indirect pathway is only 14.

3. CONCLUSION

In summary, we introduced a new method to determine the site-specific activity of nanoparticles by using PDMS microchambers. This method is particularly suitable for micrometer-sized 1D or 2D nanoparticles with high activity. Through this research, we found that the corner regions have the highest activity, followed by the edge regions and then the flat facet regions. We further studied the size effect of gold nanoplates on the site-specific activities of different regions. The site-specific activities for the flat facet and corner regions are not correlated with the size of gold nanoplates. However, the specific activity at the edge region is positively correlated with the size of the gold nanoplates. This positive correlation is due to the larger roughness of the edges for larger gold nanoplates, indicating that more defects cause higher reactivity. Furthermore, this research reveals two kinds of catalytic kinetic behaviors: a direct pathway and an indirect pathway. Most of the nanoplate regions (~89%) follow the direct pathway, while only a small fraction of the regions (~11%) follow the indirect pathway. Other advantages from the approach invented in this research include high sensitivity, low reagent consumption, reusability, and recyclability, which indicate that it can generally be used for many other types of reactions, including electrochemical and photochemical reactions.

4. MATERIALS AND EXPERIMENTS

4.1. Materials and Characterization. All commercial materials were used as received unless specified. The nanostructures of Au nanoplates were characterized by TEM (200 kV, Tecnai G2 F20 S-TWIN; FEI) and SEM (Quanta 400 FEG; FEI). The UV−vis−NIR spectra were obtained on a Shimadzu UV-1800 spectrometer. Image analyses were done using home-written MATLAB codes.

4.2. Preparation and Characterization of Gold Nanoplates. The micrometer-scale gold nanoplates were prepared by reducing $AuCl^{4-}$ with ascorbic acid in cetyltrimethylammonium bromide (CTAB) solution according to a previous report.[48] The gold nanoplates were easily separated from the mixture containing gold spherical nanoparticles and nanorods by several rounds of gravity sedimentation. The proportion of gold nanoplates can be increased from 10% to 70% after the separation procedure (purification details are given in Figure S5 in the Supporting Information). Most of the nanoplates had triangular and hexagonal shapes. Some other shapes were also observed. The size distribution of the gold nanoplates with different shapes is shown in Figure S9 in the Supporting Information. The resulting samples were characterized by UV−vis−NIR absorption spectroscopy (Figure S6 in the Supporting Information), atomic force microscopy (AFM) (Figure S8 in the Supporting Information), and transmission electron microscopy (TEM) (Figure S7 in the Supporting Information). The UV−vis−NIR absorption spectrum of the hydrosol exhibits a broad extinction band extended into the NIR region (Figure S6), thus demonstrating the formation of gold nanoplates. The average thickness of the gold nanoplates is ~30 nm, as measured by AFM (Figure S8 in the Supporting Information).

4.3. Fabrication of Femtoliter PDMS Microchamber Arrays. Femtoliter arrays were microstructured into the surface of a silica wafer by photolithography and anisotropic reactive ion etching, as described in the Supporting Information. The arrays, prepared using a master template, consisted of thousands of cylinders with a diameter of 5 μm and a depth of 5 μm, as confirmed by scanning electron microscopy (SEM) (Figure S2 in the Supporting Information). PDMS polymer base and curing agent were mixed in the ratio of 10/1 (w/w) and degassed for 0.5 h under vacuum. Next, the mixture was gently cast onto the master template and cured at 80 °C for 1 h before the polymer was peeled off. Finally, the molded PDMS slab was cut into pieces of 1.5 × 1.5 mm^2 and prepared for the microfluidic reactor cell. The microfluidic reactor cell was formed between a quartz slide onto which the gold nanoplates were adsorbed and a molded PDMS slab separated by double-sided tape. Reactant solutions consisted of 100 μM resazurin and 0.1 M NH_2OH with the pH adjusted to 7.3. To facilitate

DOI: 10.1021/acscatal.6b03518
ACS Catal. 2017, 7, 3607−3614

the catalytic reaction, the gold nanoplates on the slide were cleaned with oxygen plasma. The gold nanoplates retain their shapes after plasma treatment, as shown in Figure S10 in the Supporting Information.

4.4. Sealing of PDMS Microreactor Array. The microfluidic reactor cell was mounted under an integration of dark-field and epifluorescence microscopes. In addition, we adjusted the objective to focalize on the gold nanoplate adsorbed quartz slide. The slide and the PDMS slab were spatially separated at this moment. Then, ethanol and water were flowed in the microfluidic reactor cell successively to wash the flow cell. Finally, the reactant solutions were flowed into the flow cell and added to the PDMS microreactors. A vacuum was applied to the outlet of the microfluidic reactor cell after the reactant solutions had flowed in. Due to its characteristics of flexibility, the PDMS slab would deform and seal to the glass slide tightly. At this moment, the catalytic reaction inside the PDMS microchambers began. A schematic of the sealing process is shown in Figure S3 in the Supporting Information. The scattering signal was collected by a 40× air objective and detected by an EMCCD camera at the moment the sealing process finished. The time between the finish of the sealing and the signal acquisition was usually about 30 s.

4.5. Image Acquisition and Analysis. Individual gold nanoplates were imaged using the dark-field microscope. The scattering signal was collected by a 40× air objective and detected by an ANDOR Ixon DU-897D-CS0-#BV EMCCD camera controlled by Andor IQ software. The specific intensity was kept at ∼7 W m^{-2}. The reason for using such a low-intensity laser is to decrease the light-induced fluorescence quenching. Because we took many fluorescence images during the measurement, fluorescence quenching could be a serious problem if the laser intensity was too strong. The fluorescent signal was recorded by an EMCCD camera using an epifluorescence microscope (IX71; Olympus, Japan). A continuous-wave (∼5−10 μW) circularly polarized 532 nm laser was focused onto a ∼1 × 1.2 mm^2 area in the microfluidic reactor cell to directly excite the fluorescence of the resorufin product molecules. The fluorescence images were obtained every 1 s for 10 s with an exposure rate of 50 ms per frame. The fluorescence intensity of reaction was background corrected by subtracting the fluorescence intensity of surrounding chambers without covering gold nanoplates.

■ ASSOCIATED CONTENT

Supporting Information

The Supporting Information is available free of charge on the ACS Publications website at DOI: 10.1021/acscatal.6b03518.

Additional details on experiment design, control experiment, figures, and simulations (PDF)

■ AUTHOR INFORMATION

Corresponding Author

*E-mail for X.X.: xczhou2013@sinano.ac.cn.

ORCID

Liuming Yan: 0000-0002-2539-7476

Xiaochun Zhou: 0000-0001-9793-6072

Author Contributions

X.Z. conceived the experiments. Y.D. performed the experiments. Y.Z., S.L., Y.S. and F.N. contributed to the experiments. X.Z. and Y.D. analyzed the data and wrote the paper. X.H. contributed to analyzing the data.

Notes

The authors declare no competing financial interest.

■ ACKNOWLEDGMENTS

The authors are grateful for financial support granted by Ministry of Science and Technology of China (No. 2016YFA0200700, No. 2016YFE0105700), the National Natural Science Foundation of China (No. 21373264, No. 21573275), the Natural Science Foundation of Jiangsu Province (BK20150362), Suzhou Institute of Nanotech and Nanobionics (Y3AAA11004), and Thousand Youth Talents Plan (Y3BQA11001). We are thankful to Dr. Shaobo Xi and Dr. Haoyuan Li for the suggestions of the preparation and purification of Au nanoplates.

■ REFERENCES

(1) Nasilowski, M.; Mahler, B.; Lhuillier, E.; Ithurria, S.; Dubertret, B. *Chem. Rev.* **2016**, *116*, 10934−10982.

(2) Fan, Z. X.; Huang, X.; Tan, C. L.; Zhang, H. *Chem. Sci.* **2015**, *6*, 95−111.

(3) Butler, S. Z.; Hollen, S. M.; Cao, L. Y.; Cui, Y.; Gupta, J. A.; Gutierrez, H. R.; Heinz, T. F.; Hong, S. S.; Huang, J. X.; Ismach, A. F.; Johnston-Halperin, E.; Kuno, M.; Plashnitsa, V. V.; Robinson, R. D.; Ruoff, R. S.; Salahuddin, S.; Shan, J.; Shi, L.; Spencer, M. G.; Terrones, M.; Windl, W.; Goldberger, J. E. *ACS Nano* **2013**, *7*, 2898−2926.

(4) Sun, H.; Deng, J.; Qiu, L. B.; Fang, X.; Peng, H. S. *Energy Environ. Sci.* **2015**, *8*, 1139−1159.

(5) Niyogi, S.; Hamon, M. A.; Hu, H.; Zhao, B.; Bhowmik, P.; Sen, R.; Itkis, M. E.; Haddon, R. C. *Acc. Chem. Res.* **2002**, *35*, 1105−1113.

(6) Futaba, D. N.; Hata, K.; Yamada, T.; Hiraoka, T.; Hayamizu, Y.; Kakudate, Y.; Tanaike, O.; Hatori, H.; Yumura, M.; Iijima, S. *Nat. Mater.* **2006**, *5*, 987−994.

(7) Sun, Y. P.; Fu, K. F.; Lin, Y.; Huang, W. J. *Acc. Chem. Res.* **2002**, *35*, 1096−1104.

(8) Sofo, J. O.; Chaudhari, A. S.; Barber, G. D. *Phys. Rev. B: Condens. Matter Mater. Phys.* **2007**, *75*, 153401.

(9) Katsnelson, M. I. *Mater. Today* **2007**, *10*, 20−27.

(10) Wang, H. T.; Yuan, H. T.; Hong, S. S.; Li, Y. B.; Cui, Y. *Chem. Soc. Rev.* **2015**, *44*, 2664−2680.

(11) Chen, X.; McDonald, A. R. *Adv. Mater.* **2016**, *28*, 5738−5746.

(12) Lv, R.; Robinson, J. A.; Schaak, R. E.; Sun, D.; Sun, Y. F.; Mallouk, T. E.; Terrones, M. *Acc. Chem. Res.* **2015**, *48*, 56−64.

(13) El-Sayed, M. A. *Acc. Chem. Res.* **2001**, *34*, 257−264.

(14) Millstone, J. E.; Hurst, S. J.; Metraux, G. S.; Cutler, J. I.; Mirkin, C. A. *Small* **2009**, *5*, 646−664.

(15) Hong, X.; Tan, C. L.; Chen, J. Z.; Xu, Z. C.; Zhang, H. *Nano Res.* **2015**, *8*, 40−55.

(16) Hernandez-Alonso, M. D.; Fresno, F.; Suarez, S.; Coronado, J. M. *Energy Environ. Sci.* **2009**, *2*, 1231−1257.

(17) Tang, J. W.; Durrant, J. R.; Klug, D. R. *J. Am. Chem. Soc.* **2008**, *130*, 13885−13891.

(18) Bhattacharrya, S.; Saha, S. K.; Chakravorty, D. *Appl. Phys. Lett.* **2000**, *76*, 3896−3898.

(19) Zhang, R.; Zhang, Y.; Zhang, Q.; Xie, H.; Qian, W.; Wei, F. *ACS Nano* **2013**, *7*, 6156−6161.

(20) Jiu, J.; Suganuma, K.; Nogi, M. *J. Mater. Sci.* **2011**, *46*, 4964−4970.

(21) Moon, G. D.; Lim, G.-H.; Song, J. H.; Shin, M.; Yu, T.; Lim, B.; Jeong, U. *Adv. Mater.* **2013**, *25*, 2707−2712.

(22) Lee, C.-L.; Chiou, H.-P.; Syu, C.-M.; Liu, C.-R.; Yang, C.-C.; Syu, C.-C. *Int. J. Hydrogen Energy* **2011**, *36*, 12706−12714.

(23) Tian, Z. Q.; Lim, S. H.; Poh, C. K.; Tang, Z.; Xia, Z.; Luo, Z.; Shen, P. K.; Chua, D.; Feng, Y. P.; Shen, Z.; Lin, J. *Adv. Energy Mater.* **2011**, *1*, 1205−1214.

(24) Sherrell, P. C.; Zhang, W.; Zhao, J.; Wallace, G. G.; Chen, J.; Minett, A. I. *ChemSusChem* **2012**, *5*, 1233−1240.

DOI: 10.1021/acscatal.6b03518
ACS Catal. 2017, 7, 3607−3614

(25) Yuan, W.; Cheng, Y.; Shen, P. K.; Li, C. M.; Jiang, S. P. *J. Mater. Chem. A* **2015**, *3*, 1961−1971.
(26) Miao, Z.; Xu, D. S.; Ouyang, J. H.; Guo, G. L.; Zhao, X. S.; Tang, Y. Q. *Nano Lett.* **2002**, *2*, 717−720.
(27) Sheng, X.; Chen, L.; Xu, T.; Zhu, K.; Feng, X. *Chem. Sci.* **2016**, *7*, 1910−1913.
(28) Liu, G.; Sun, C. H.; Yang, H. G.; Smith, S. C.; Wang, L. Z.; Lu, G. Q.; Cheng, H. M. *Chem. Commun.* **2010**, *46*, 755−757.
(29) Xi, S.; Liu, X.; He, T.; Tian, L.; Wang, W.; Sun, R.; He, W.; Zhang, X.; Zhang, J.; Ni, W.; Zhou, X. *Nanoscale* **2016**, *8*, 12029−12034.
(30) Bansal, V.; Jani, H.; Du Plessis, J.; Coloe, P. J.; Bhargava, S. K. *Adv. Mater.* **2008**, *20*, 717−723.
(31) Xu, W. L.; Shen, H.; Kim, Y. J.; Zhou, X. C.; Liu, G. K.; Park, J.; Chen, P. *Nano Lett.* **2009**, *9*, 3968−3973.
(32) Zhou, X. C.; Andoy, N. M.; Liu, G. K.; Choudhary, E.; Han, K. S.; Shen, H.; Chen, P. *Nat. Nanotechnol.* **2012**, *7*, 237−241.
(33) Wang, W. H.; Gu, J. N.; He, T.; Shen, Y. B.; Xi, S. B.; Tian, L.; Li, F. F.; Li, H. Y.; Yan, L. M.; Zhou, X. C. *Nano Res.* **2015**, *8*, 441−455.
(34) Goldsmith, B. R.; Coroneus, J. G.; Kane, A. A.; Weiss, G. A.; Collins, P. G. *Nano Lett.* **2008**, *8*, 189−194.
(35) Tachikawa, T.; Majima, T. *Chem. Soc. Rev.* **2010**, *39*, 4802−4819.
(36) Tachikawa, T.; Majima, T. *J. Am. Chem. Soc.* **2009**, *131*, 8485−8495.
(37) Tachikawa, T.; Yamashita, S.; Majima, T. *J. Am. Chem. Soc.* **2011**, *133*, 7197−7204.
(38) Weckhuysen, B. M. *Angew. Chem., Int. Ed.* **2009**, *48*, 4910−4943.
(39) Li, R.; Zhang, F.; Wang, D.; Yang, J.; Li, M.; Zhu, J.; Zhou, X.; Han, H.; Li, C. *Nat. Commun.* **2013**, *4*, 1432.
(40) Andoy, N. M.; Zhou, X. C.; Choudhary, E.; Shen, H.; Liu, G. K.; Chen, P. *J. Am. Chem. Soc.* **2013**, *135*, 1845−1852.
(41) De Cremer, G.; Roeffaers, M. B. J.; Bartholomeeusen, E.; Lin, K.; Dedecker, P.; Pescarmona, P. P.; Jacobs, P. A.; De Vos, D. E.; Hofkens, J.; Sels, B. F. *Angew. Chem., Int. Ed.* **2010**, *49*, 908−911.
(42) Roeffaers, M. B. J.; De Cremer, G.; Libeert, J.; Ameloot, R.; Dedecker, P.; Bons, A.-J.; Bueckins, M.; Martens, J. A.; Sels, B. F.; De Vos, D. E.; Hofkens, J. *Angew. Chem., Int. Ed.* **2009**, *48*, 9285−9289.
(43) Ha, J. W.; Ruberu, T. P. A.; Han, R.; Dong, B.; Vela, J.; Fang, N. *J. Am. Chem. Soc.* **2014**, *136*, 1398−1408.
(44) Rondelez, Y.; Tresset, G.; Tabata, K. V.; Arata, H.; Fujita, H.; Takeuchi, S.; Noji, H. *Nat. Biotechnol.* **2005**, *23*, 361−365.
(45) Rondelez, Y.; Tresset, G.; Nakashima, T.; Kato-Yamada, Y.; Fujita, H.; Takeuchi, S.; Noji, H. *Nature* **2005**, *433*, 773−777.
(46) Sims, P. A.; Greenleaf, W. J.; Duan, H.; Xie, S. *Nat. Methods* **2011**, *8*, 575−580.
(47) Iino, R.; Hayama, K.; Amezawa, H.; Sakakihara, S.; Kim, S. H.; Matsumono, Y.; Nishino, K.; Yamaguchi, A.; Noji, H. *Lab Chip* **2012**, *12*, 3923−3929.
(48) Heo, J.; Lee, Y. W.; Kim, M.; Yun, W. S.; Han, S. W. *Chem. Commun.* **2009**, 1981−1983.
(49) Lee, H.; Habas, S. E.; Kweskin, S.; Butcher, D.; Somorjai, G. A.; Yang, P. *Angew. Chem., Int. Ed.* **2006**, *45*, 7824−7828.
(50) Shahabi, H. H.; Ratnam, M. M. *Int. J. Adv. Manuf. Technol.* **2010**, *48*, 213−226.
(51) Jain, S.; Udgaonkar, J. B. *Biochemistry* **2011**, *50*, 1153−1161.
(52) Wunder, S.; Lu, Y.; Albrecht, M.; Ballauff, M. *ACS Catal.* **2011**, *1*, 908−916.
(53) Nimlos, M. R.; Wolfrum, E. J.; Brewer, M. L.; Fennell, J. A.; Bintner, G. *Environ. Sci. Technol.* **1996**, *30*, 3102−3110.
(54) Shen, H.; Zhou, X.; Zou, N.; Chen, P. *J. Phys. Chem. C* **2014**, *118*, 26902−26911.
(55) Li, M.; Chen, G. *Nanoscale* **2013**, *5*, 11919−11927.
(56) Li, M.; Chen, G.; Bhuyain, S. *Nanoscale* **2015**, *7*, 2641−2650.

DOI: 10.1021/acscatal.6b03518
ACS Catal. 2017, 7, 3607−3614